Salt Feedback in the Adiabatic Overturning Circulation

CHRISTOPHER L. WOLFE* AND PAOLA CESSI

Scripps Institution of Oceanography, University of California, San Diego, La Jolla, California

ABSTRACT

The adiabatic overturning circulation is the part of the meridional overturning circulation that persists in the limit of vanishing diffusivity. Two conditions are required for the existence of the adiabatic overturning circulation: a high-latitude zonally reentrant channel subject to surface westerlies and a set of outcropping isopycnals shared between the channel and the opposite hemisphere. This paper examines how different buoyancy forcing regimes, particularly freshwater flux, affect the surface buoyancy distribution and the strength of the adiabatic overturning circulation. Without freshwater forcing, salinity is uniform and buoyancy is determined by temperature only. In this case, the size of the shared isopycnal window is effectively fixed by the coupling between atmospheric and sea surface temperatures. With freshwater forcing (applied as a surface flux), the salinity, and thus the sea surface buoyancy and the size of the shared isopycnal window, is not specified by the atmospheric state alone. It is found that a salt–advection feedback leads to surface buoyancy distributions that increase the size of the isopycnal window and strengthen the adiabatic overturning circulation. The strength of the feedback is controlled by processes in high latitudes—the southern channel, where the surface salinity is determined by a balance between freshwater input from the atmosphere, salt input from upwelling deep water, and freshwater export by Ekman transport; and the Northern Hemisphere, where the overturning and wind-driven transport in the thermocline advect salty water from the subtropics, mitigating the freshening effect of the surface freshwater flux. The freshwater budget in the channel region provides an estimate of the size of the isopycnal window.

1. Introduction

The meridional heat transport in the ocean is not symmetric about the equator—the peak northward heat flux in the Northern Hemisphere (NH) is about twice the peak southward heat flux in the Southern Hemisphere (SH; Fasullo and Trenberth 2008), even though there is 30% more ocean in the SH than in the NH. This asymmetry is due in part to the fact that the heat transport in the Atlantic Ocean is northward at every latitude north of 30°S (Trenberth and Fasullo 2008). The northward Atlantic heat transport partially compensates for some of the southward Indo-Pacific heat flux in the SH, leading to a reduced poleward heat flux in this hemisphere.

The northward heat flux in the Atlantic Ocean is due primarily to the Atlantic meridional overturning circulation (AMOC; Bryden and Imawaki 2001), wherein cold water masses [collectively known as North Atlantic Deep Water (NADW)] formed in the seas surrounding Greenland flow southward at depth along the western boundary of the Atlantic Ocean toward the Southern Ocean, where they are distributed to the other ocean basins by the Antarctic Circumpolar Current (ACC; Gordon 1986). This cold outflow at depth is returned to the North Atlantic as a warm surface current; the resulting circulation exports cold water and imports warm water at all latitudes, leading to a net northward heat flux (Roemmich and Wunsch 1985). The excess heat transported by the AMOC is returned to the atmosphere in the relatively small North Atlantic Ocean and has a significant impact on the climate of the countries bordering the North Atlantic. It is therefore important that the mechanisms supporting the AMOC and its variability be understood if the regional climate of the North Atlantic is to be predicted.

The route by which NADW exported from the Atlantic Ocean transforms into the warm return flow is not

*Current affiliation: School of Marine and Atmospheric Sciences, Stony Brook University, Stony Brook, New York.

Corresponding author address: Christopher L. Wolfe, School of Marine and Atmospheric Sciences, Stony Brook University, Stony Brook, NY 11794-5000.
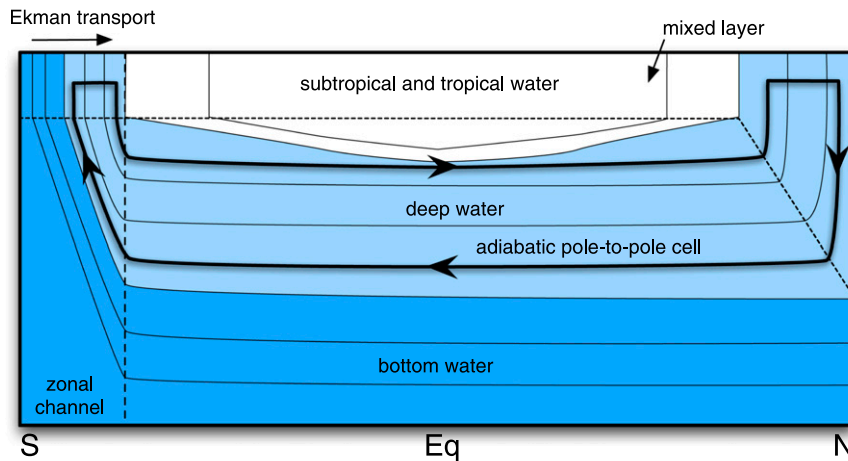E-mail: christopher.wolfe@stonybrook.edu

FIG. 1. Schematic of the adiabatic overturning circulation. Thin lines give the zonally averaged isopycnal height, and thick solid lines show the adiabatic pole-to-pole cell. Figure is adapted from Wolfe and Cessi (2011).

known with certainty and is a subject of current research (Gordon 1986; Rintoul 1991; Marshall and Speer 2012). Classical models of the AMOC envisaged the NADW upwelling through the tropical and subtropical thermoclines, balanced by a downward turbulent mixing of warm water (Robinson and Stommel 1959; Stommel and Arons 1959a,b; Munk 1966; Munk and Wunsch 1998). Given the observed stratification and deep-water formation rates, the diffusivity κ required to support a diffusive AMOC was estimated to be $\kappa \approx 10^{-4}\,\mathrm{m^2\,s^{-1}}$ (Munk 1966; Munk and Wunsch 1998). Direct measurements of the ocean's turbulent diffusivity using microstructure probes or dispersion of tracers are still too sparse to make definitive estimates of κ in the depth range occupied by the NADW (approximately 1000–3000 m), but estimates of κ using both shear (measured by acoustic Doppler current profilers) and strain (measured by conductivity–temperature–depth samplers) suggest that κ may be too small—by as much as a factor of 10—to support a diffusive AMOC (Kunze et al. 2006), although hot spots, especially in the Southern Ocean, might increase this estimate (Garabato et al. 2004).

This "missing mixing" problem prompted the oceanographic community to consider models of the AMOC that do not require large values of κ in the ocean interior. Toggweiler and Samuels (1998) noted that the AMOC could be sustained in the limit of zero interior diffusivity in domains with a zonally reentrant southern channel subject to surface westerlies. Net (i.e., zonally integrated) geostrophically balanced meridional flow is forbidden in zonally reentrant geometries, as the net pressure gradient vanishes. This means that net meridional flow can only be found in the channel within Ekman layers or below the level of the highest topography

(Vallis 2000). If the level of the highest topography is located below the depth range of the deep water—as it is in the modern World Ocean—water driven north in the Ekman layer can only be replaced by deep water mechanically upwelled by Ekman suction. Toggweiler and Samuels (1995) called this the "Drake Passage effect." Subsequent authors have used this result, extended to account for the effects of mesoscale eddies in the Southern Ocean, to build conceptual models of the AMOC that do not require large values of κ in the ocean's interior (Wolfe and Cessi 2010, 2011; Radko and Kamenkovich 2011; Nikurashin and Vallis 2012).

A recent conceptual model of the adiabatic overturning circulation is illustrated in Fig. 1. This schematic gives an idealized, zonally averaged[1] representation of the stratification and residual overturning circulation in a single-basin ocean with a zonally reentrant southern channel (representative of the ACC). The ocean is assumed to be nearly adiabatic beneath a diabatic surface mixed layer that is thin compared to the total depth of the ocean. Isopycnals (thin lines) are divided into three classes:

(i) isopycnals that do not outcrop in the channel (white fill), which are associated with the main subtropical and tropical thermoclines;
(ii) isopycnals that outcrop only in the channel (dark blue fill), which are associated with bottom water formed in the southern subpolar areas; and
(iii) isopycnals that outcrop both in the channel and the northern subpolar region (light blue fill), which we

---

[1] The zonal average is taken at constant buoyancy.

term "shared." These isopycnals are associated with deep water formed in the high northern latitudes.

On the shared isopycnals, an adiabatic pole-to-pole circulation (thick black line) can be maintained by deep-water formation in the northern subpolar regions. Once this deep water leaves the mixed layer, it slides adiabatically to the southern channel, where it is upwelled mechanically by deep-reaching Ekman suction driven by surface westerlies, partially canceled by a contribution from eddy buoyancy transport in the channel. Once at the surface, water parcels are driven across isopycnals by northward Ekman transport and diabatic eddy fluxes. Once they reach the northern edge of the channel, water parcels can proceed north either by subducting below the mixed layer and returning adiabatically (as shown in Fig. 1) or by remaining in the mixed layer; which route dominates is currently not known. Once the water parcels return to the surface in the northern subpolar gyre (NSG), they are again driven northward across isopycnals—this time by the gyral circulation—and the loop is closed.

The necessary ingredients for the adiabatic pole-to-pole cell are thus a circumpolar channel subjected to surface westerlies, which allows the wind-driven circulation to penetrate to great depth, and a set of isopycnals outcropping in both the channel and the NH. The pole-to-pole cell is driven, in an energetic sense, mechanically by wind over the channel (Wunsch 1998; Ferrari and Wunsch 2009), but is enabled by buoyancy fluxes that maintain the shared isopycnals in both hemispheres. If the northern subpolar waters became too light or the channel waters became too dense, the shared window would vanish and the pole-to-pole cell would collapse. This paradigm is opposite the classical view of the meridional overturning circulation (formerly known as the thermohaline circulation) where the pole-to-pole flow is powered by buoyancy differences between the hemispheres and diapycnal mixing (Rooth 1982). Implicit evidence of the "shared surface buoyancy" mechanism has been given in model experiments, where the AMOC has been found to strengthen in response to increased buoyancy in the ACC (Weaver et al. 2003; Knorr and Lohmann 2003).

The ocean interior is unlikely to be perfectly adiabatic. Weak mixing can support diabatic overturning cells involving deep-water formation at high latitudes balanced by diffusive upwelling in the tropics and subtropics. The diabatic cells circulate in the same direction as the adiabatic cell (clockwise) in the NH and in the opposite direction (anticlockwise) in the SH. Thus, superposing the adiabatic and diabatic cells produces an asymmetric AMOC that is stronger in the NH than in the SH (Kuhlbrodt et al. 2007). Mixing and wind forcing near the surface can additionally support diabatic surface cells in the tropics and subtropics; bottom-intensified mixing can support a diffusively driven deep overturning cell associated with bottom water. These latter overturning circulations are not the focus of the present study.

If the density of seawater depended only on temperature, the surface density distribution—and hence, the size of the shared isopycnal window—would be approximately specified by prescribing the atmospheric state because, over large spatial scales and long time scales, oceanic and atmospheric temperatures are tightly coupled at the sea surface (Haney 1971). In contrast, precipitation is not strongly influenced by ocean salinity, and the freshwater exchange at the air–sea interface results in a prescribed surface freshwater flux rather than a prescribed salinity. Thus, with salt, the surface buoyancy distribution is not known by prescribing the atmospheric state, but is rather part of the resulting circulation. Several authors (Stommel 1961; Bryan 1986; Cessi and Young 1992; Rahmstorf 1996) have pointed out that the salt distribution is such as to increase the buoyancy differences between the meridional end points of the overturning cell, leading to a positive salt feedback in diffusive models of the AMOC, whereby the advection of salt in the region of freshening leads to an increase in the density difference between the end points of the circulation, which in turn leads to an increase in the strength of the overturning. However, we show that in the adiabatic regime, the positive salt feedback still exists, but acts to decrease the buoyancy differences between the meridional end points of the overturning cell, while increasing the range of shared surface buoyancies: it is a positive feedback because it reinforces the residual overturning.

More generally, the purpose of this paper is to examine the role of buoyancy forcing, and in particular of the freshwater flux, in the adiabatic overturning circulation through a series of idealized process studies using an oceanic general circulation model. The model is described in section 2 and some frequently used diagnostics are introduced in section 3. As a prelude, section 4 examines the response of the overturning circulation to changes in surface temperature forcing in the absence of freshwater forcing. The effect of salt forcing on the overturning circulation and stratification is examined in section 5. A scaling law that explains the relationship of the strength of the pole-to-pole overturning circulation and stratification to the size of the shared isopycnal window is discussed in section 6, and the geography of salt transport is considered in section 7. Finally, the results are summarized in section 8.
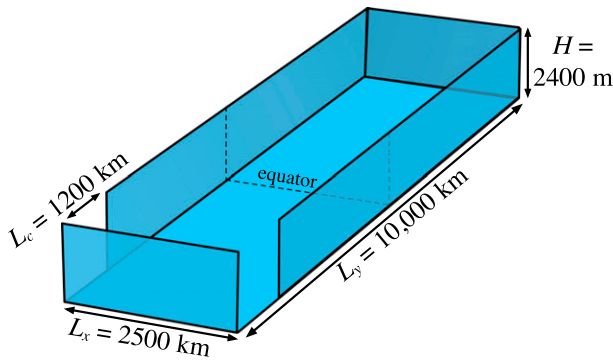
FIG. 2. Model domain.

2. Model description

We use the Massachusetts Institute of Technology General Circulation Model (MITgcm; Marshall et al. 1997a,b) to integrate the hydrostatic Boussinesq primitive equations in a rectangular, equatorially centered domain with zonal and meridional extents of $L_x = 2500$ km and $2L_y = 10\,000$ km, respectively, and a depth of $H = 2400$ m.[2] The model has a flat bottom and vertical walls, except for the range $-L_y \leq y \leq y_c$, where $y_c = -3750$ km, which is a flat-bottomed, zonally reentrant channel. We employ the β-plane approximation, where $\beta = 2.3 \times 10^{-11}\,\mathrm{m^{-1}\,s^{-1}}$. The model domain is shown in Fig. 2. The horizontal resolution is 100 km. There are $N_z = 20$ levels in the vertical with thicknesses ranging from 12 m near to the surface to 225 m near the bottom. The level interfaces are located at

$$z_k = -H\left[1 - \frac{\tanh\lambda(N_z - k)}{\tanh\lambda N_z}\right] \quad \text{for} \quad k = 0, \ldots, N_z,$$

(1)

where $\lambda = 0.11$.

Momentum is dissipated via Laplacian viscosity with horizontal and vertical coefficients $A_h = 10^4\,\mathrm{m^2\,s^{-1}}$ and $A_v = 2.5 \times 10^{-4}\,\mathrm{m^2\,s^{-1}}$, respectively; we employ no-slip sidewalls and a free-slip bottom augmented by a linear bottom drag with coefficient $r = 5 \times 10^{-6}\,\mathrm{s^{-1}}$. Eddies are parameterized using the advective form of Gent and McWilliams (1990, hereafter GM) and Redi (1982) isopycnal mixing with equal mixing coefficients

$\kappa_e = 500\,\mathrm{m^2\,s^{-1}}$; this value was determined by matching the slopes in the model's channel with those from an eddy-resolving simulation in the same domain (Wolfe and Cessi 2011). GM is implemented using the boundary value problem (BVP) scheme of Ferrari et al. (2010) with vertical mode number $m = 2$ and minimum wave speed $c_{\min} = 0.1\,\mathrm{m\,s^{-1}}$. The Redi tensor is tapered exponentially to horizontal diffusion in regions of weak stratification using the method of Danabasoglu and McWilliams (1995).

Tracers are advected using a flux-limited form of the Prather (1986) second-order moments scheme, which allows explicit horizontal diffusivities to be set to zero while maintaining model stability. Vertical diffusivity is surface intensified to model an idealized mixed layer of specified depth $d = 40$ m and has the form

$$\kappa_v(z) = \kappa_a + \frac{1}{2}\kappa_s\left(1 + \tanh\frac{z + d}{\delta_{\mathrm{mix}}}\right),$$

(2)

where $\delta_{\mathrm{mix}} = 5$ m and the surface diffusivity $\kappa_s = 5 \times 10^{-3}\,\mathrm{m^2\,s^{-1}}$. The mixed-layer diffusivity is large enough that the results are insensitive to $O(1)$ changes in its amplitude (Wolfe and Cessi 2011). The advantage of the choice (2) is that it is simple and the mixed-layer depth is known (except at high latitudes, where convective adjustment is active). Two values for the abyssal diffusivity are considered: a moderate-diffusivity (MOD-DIFF) case with $\kappa_a = 2.5 \times 10^{-5}\,\mathrm{m^2\,s^{-1}}$ and a low-diffusivity (LOW-DIFF) case with $\kappa_a = 3.125 \times 10^{-6}\,\mathrm{m^2\,s^{-1}}$.[3] The implicit diffusivity of Prather's advection scheme is below the lowest abyssal vertical diffusivity used in our computations. Profiles of the two diffusivities are shown in Fig. 3.

We employ a linear equation of state, so that buoyancy is given by

$$b = g\alpha_\theta(\theta - \theta_{\mathrm{ref}}) - g\beta_S(S - S_{\mathrm{ref}}),$$

(3)

where θ is potential temperature, $\theta_{\mathrm{ref}} = 0.5°\mathrm{C}$, S is salinity, $S_{\mathrm{ref}} = 35$ psu, g is gravitational acceleration, and the expansion coefficients are $\alpha_\theta = 2 \times 10^{-4}\,\mathrm{K^{-1}}$ and $\beta_S = 7.5 \times 10^{-4}\,\mathrm{psu^{-1}}$.

The surface forcing functions are idealized representations of the forcing of the Atlantic Ocean and are

---

[2] This is roughly half the size, in all dimensions, of the Atlantic Ocean. This domain size was chosen to match an eddy-resolving model used in earlier studies (Wolfe et al. 2008; Cessi and Wolfe 2009; Wolfe and Cessi 2009; Cessi et al. 2010; Wolfe and Cessi 2010, 2011); computational limitations required that the eddy-resolving model be run in a relatively small domain.

[3] The parameter that measures the effect of diffusion on the flow is the ratio of the vertical Ekman and Prandtl numbers, $\mathrm{Ek}_v/\sigma_v = \kappa_a/f_0 H^2$. For fixed rotation rate f_0 and aspect ratio H/L, diffusivity must scale quadratically with the domain size to keep Ek_v/σ_v constant. Thus the moderate and low diffusivities correspond to $\kappa_a = 1 \times 10^{-4}\,\mathrm{m^2\,s^{-1}}$ and $\kappa_a = 1.25 \times 10^{-5}\,\mathrm{m^2\,s^{-1}}$, respectively, for an Atlantic-sized basin.
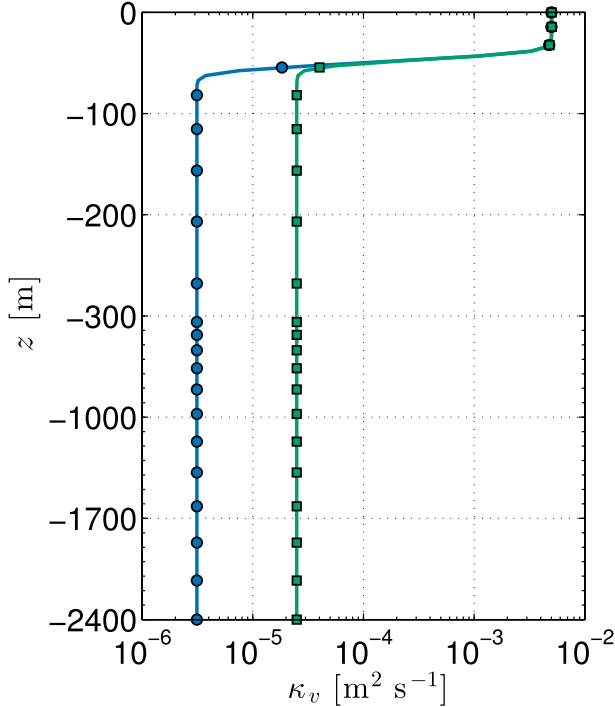
FIG. 3. Profiles of vertical diffusivity κ_v for the LOW-DIFF (blue circles) and MOD-DIFF (green squares) experiments. Filled symbols give the diffusivities at the vertical grid points. Note the change in vertical scale below 300 m.

FIG. 4. (a) Wind stress τ, (b) SST relaxation profile $T^\star$, and (c) precipitation minus evaporation $P - E$ (used in the SALT experiments only), as a function of meridional position y. The gray shading gives the lat band of the channel. In (b), the envelope of possible temperature profiles is given; the horizontal dashes denote the temperature at the northern edge of the channel.

shown in Fig. 4. Wind stress is purely zonal and is given by

$$\tau(y) = \tau_0 \left(-\cos\frac{3\pi y}{2L_y} + a_\tau e^{-y^2/\delta_\tau^2} \right), \qquad (4)$$

where $\tau_0 = 0.1$ Pa, $a_\tau = 0.8$, and $\delta_\tau = 640$ km. The sea surface temperature (SST) is relaxed with a time scale of 8.8 days to the profile

$$T^\star(y) = T_{\text{eq}}^\star \cos^2\frac{\pi y}{2L_y} + T_N^\star e^{-(y-L_y)^2/\delta_T^2}, \qquad (5)$$

where $T_{\text{eq}}^\star = 20°C$ is the temperature at the equator, $\delta_T = 1800$ km, and the temperature at the northern boundary $T_N^\star$ ranges from $0°$ to $5°C$. The short relaxation time scale is consistent with the estimate of Haney (1971) and the thickness (14 m) of the first tracer layer; it also ensures that the surface temperature is nearly clamped to the relaxation profile.

Freshwater forcing is represented by a virtual salt flux

$$\mathcal{F}(S) = -S_{\text{ref}}(P - E - \langle P - E \rangle), \qquad (6)$$
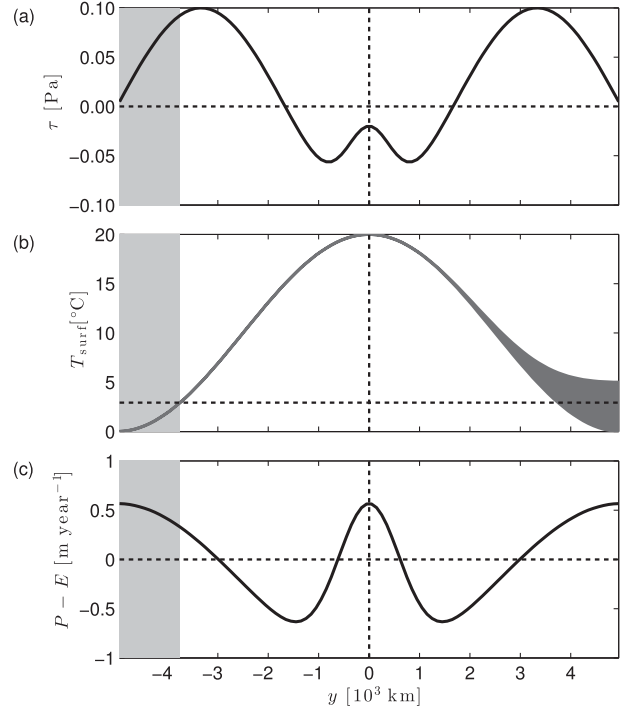
where

$$P - E = -F_0 \left(\cos\frac{\pi y}{L_y} - a_S e^{-y^2/\delta_S^2} \right), \qquad (7)$$

where P is the precipitation, E is the evaporation, $a_S = 2$, $\delta_S = 900$ km, and $\langle P - E \rangle$ is the area average of $P - E$. Positive salt fluxes are salinifying. Two values of F_0 are used: $F_0 = 0$ for the NO-SALT experiments and $F_0 = 0.81$ m yr^{-1} for the SALT experiments.

All simulations were run to statistical equilibrium—at least 5000 years—and the analyses were performed on the final 1000 years.

3. Diagnostics

a. Residual overturning streamfunction

The overturning circulation is quantified using the zonally integrated residual overturning streamfunction

$$\psi(y, \tilde{b}) \equiv \int_{-H}^{0} \overline{v^\dagger \mathcal{H}[b(x, y, z, t) - \tilde{b}]} \, dz, \qquad (8)$$

where

$$\overline{\bullet} \equiv \frac{1}{T} \int_0^T \int_0^{L_x} \bullet \, dx \, dt \qquad (9)$$

is a combined temporal average and zonal integral, $T = 1000$ yr, $v^{\dagger} = v + v_{\mathrm{GM}}$ is the total meridional velocity (the sum of the resolved velocity v and the eddy velocity from the GM parameterization v_{GM}), and $\mathcal{H}$ is the Heaviside step function. The variable ψ is the zonally integrated transport of water above the isopycnal $b(x, y, z, t) = \tilde{b}$. The "vertical" coordinate $\tilde{b}$ is the buoyancy; the tilde distinguishes the coordinate "buoyancy" from the buoyancy field (Young 2012).

As this study is concerned with the pole-to-pole component of the overturning circulation [analogous to the "push–pull" mode of Radko et al. (2008)], we quantify the strength of the overturning circulation using $\psi_{\max}$, the maximum value of ψ at the equator. Using the equatorial maximum of ψ avoids the recirculating part of the overturning circulation confined to one hemisphere, which is diffusively driven and largely insensitive to the dynamics of the channel (Griesel and Maqueda 2006).

For presentation purposes, ψ is remapped into height coordinates using the mean isopycnal height

$$\zeta(y, \tilde{b}) \equiv -\frac{1}{L_x} \int_{-H}^0 \overline{\mathcal{H}[b(x, y, z, t) - \tilde{b}]} \, dz. \qquad (10)$$

In height coordinates, ψ advects a modified buoyancy $b^{\sharp}(y, z)$ that satisfies $\zeta[y, b^{\sharp}(y, z)] = z$; that is, ψ is constant on $b^{\sharp}$ contours for purely adiabatic flow.

In the presence of zonal buoyancy gradients, the remapping distorts the vertical extent of the mixed layer. We define an isopycnal labeled by $\tilde{b}$ to be in the mixed layer if

$$\overline{\mathcal{H}(\tilde{b} - b_0 + \delta b)} \geq 0, \qquad (11)$$

where b_0 is the surface buoyancy and $\delta b = 3 \times 10^{-4}\,\mathrm{m\,s^{-2}}$ is a small threshold; the mixed-layer region is remapped into height coordinates in the same manner as ψ.

b. Thickness-weighted average salinity

The thickness-weighted average (TWA) salinity $\hat{S}$ is time and zonally averaged at constant buoyancy (Young 2012). It is defined as

$$\hat{S}(y, \tilde{b}) \equiv \frac{1}{\sigma L_x} \int_{-H}^0 \overline{S \delta(b - \tilde{b})} \, dz, \qquad (12)$$

where the thickness weight $\sigma \equiv \partial_{\tilde{b}} \zeta$ and δ is the δ function. The term $\hat{S}$ is remapped into height coordinates in the same manner as ψ.

4. NO-SALT results

a. Case study

We first describe a specific case in detail to orient the discussion of the general results. The experiments under consideration have $T_N^{\star} = 1°C$. The temperature forcing is such that the NH is warmer than the SH, but still within the range of the channel surface temperatures, as in the present-day Atlantic Ocean. Based on the temperature relaxation profile, the range of shared surface isotherms implied by the temperature relaxation profile is $\Delta T \equiv T_c^{\star} - T_N^{\star} = 1.9°C$, where $T_c^{\star} \equiv T^{\star}(y_c)$ is the relaxation temperature at the northern edge of the channel; the actual range of shared surface isotherms may differ from ΔT due to the internal dynamics. This definition of ΔT assumes that the northernmost temperature is higher than the southernmost temperature, so increasing $T_N^{\star}$ causes ΔT to decrease.

The overturning circulation and stratification for the MOD-DIFF and LOW-DIFF cases are shown in Figs. 5a and 5b, respectively. The model's AMOC occupies the middepth region, with stronger, wind-driven equatorial cells above and a weak, diffusively driven cell below. The flow below the mixed layer is less diabatic than in the mixed layer, though significant cross-isopycnal flow is present in the MOD-DIFF case. In contrast, the flow beneath the mixed layer is nearly adiabatic in the LOW-DIFF case—ψ is nearly constant on isolines of $b^{\sharp}$, except for a diffusive cell in the NH. The middepth cell stretches from the NH to the channel with a cross-equatorial flow of about 2.7 Sverdrups (Sv; $1\,\mathrm{Sv} \equiv 10^6\,\mathrm{m^3\,s^{-1}}$) in the MOD-DIFF case and 2.0 Sv in the LOW-DIFF case.

In the MOD-DIFF case, the isopycnals $1.3 \times 10^{-3} \leq b \leq 6.3 \times 10^{-3}\,\mathrm{m\,s^{-2}}$ (corresponding to $1.2° \leq \theta \leq 3.7°C$) are shared between the NH and the channel; the southward flow of the middepth cell occurs on these isopycnals. The shared buoyancies in the LOW-DIFF case are slightly different: $1.2 \times 10^{-3} \leq b \leq 6.2 \times 10^{-3}\,\mathrm{m\,s^{-2}}$ (corresponding to $1.1° \leq \theta \leq 3.7°C$). Note that the range of shared isotherms in both cases is $2.6°$ which is larger than $\Delta T = 1.9°C$. This is due to the poleward advection of warm water along the eastern boundary in the southern subpolar gyre that leads to a zonal temperature asymmetry at the northern edge of the channel (Fig. 6). Thus, the warmest water in the channel is about $T_0 \equiv 0.7°C$ warmer than $T^{\star}$ alone.

b. Variable ΔT

A suite of experiments was performed with the northernmost temperature $T_N^{\star}$ varying from $0°$ to $5°C$. The results are presented in terms of ΔT, the range of surface temperatures shared between the channel and the NH based on the surface forcing.
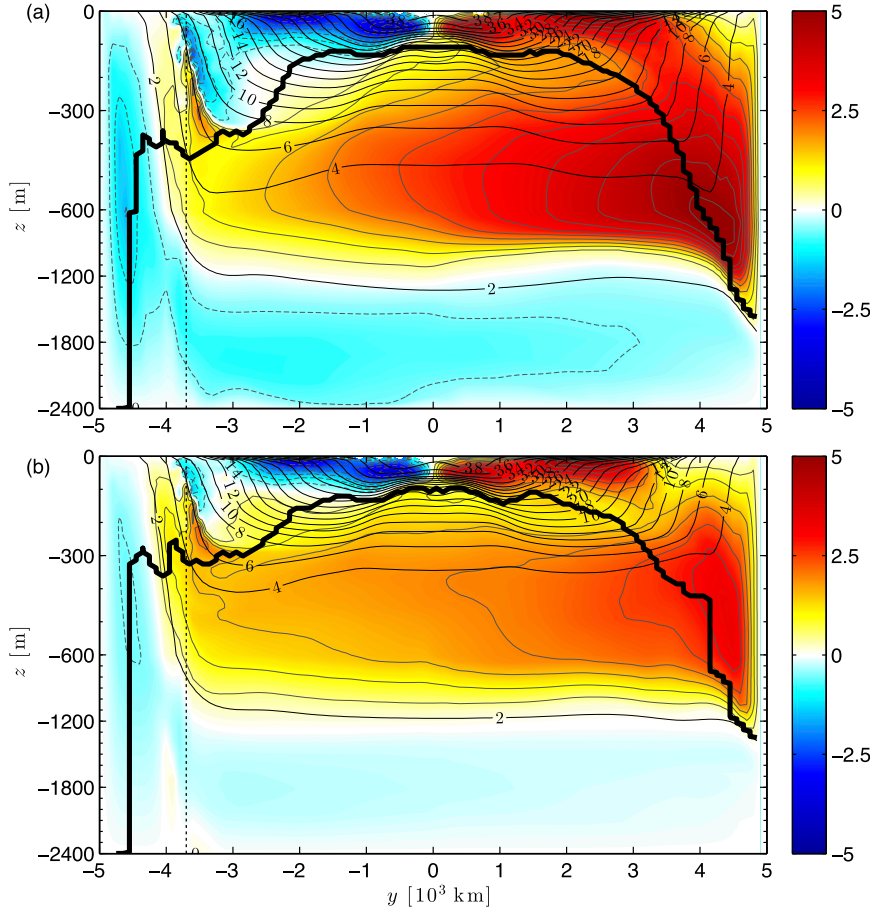
FIG. 5. Overturning streamfunction ψ (colors and gray lines; interval is 0.25 Sv) and modified buoyancy $b^{\sharp}$ (black lines; 10^{-3} m s^{-2}) for the (a) MOD-DIFF NO-SALT and (b) LOW-DIFF NO-SALT cases with $\Delta T = 1.9°$C. The thick black line gives an estimate of the base of the mixed layer. The vertical dashed line gives the northern boundary of the channel.

The strength of the overturning circulation (quantified by ψ_{max}, the maximum of ψ at the equator,[4] which—if nonzero—is found on the shared isopycnals) increases with increasing ΔT (green lines in Fig. 7a). For most values of ΔT, ψ_{max} is larger and increases faster with ΔT for the MOD-DIFF case than the LOW-DIFF case. The fact that $\psi_{max} > 0$ for $\Delta T < 0$ is due to advection of warm water along the eastern boundary into the channel, as discussed in the previous section.

The observed width (in buoyancy units) of the shared surface isopycnal window is given by

$$\Delta b \equiv \max[b_c - \max(b_S, b_N), 0], \quad (13)$$

where

$$b_S \equiv \min_{y<0} b(x, y, 0),$$

$$b_c \equiv \max_{y \leq y_c} b(x, y, 0), \quad \text{and}$$

$$b_N \equiv \min_{y>0} b(x, y, 0). \quad (14)$$

Thus, b_S and b_N are the minimum surface buoyancies in the SH and NH, respectively, and b_c is the maximum surface buoyancy found in the channel. If $b_N > b_S$ (as is the case for all NO-SALT experiments), then $\Delta b = \max(b_c - b_N, 0)$ and Δb is analogous to ΔT except that Δb is nonnegative. If no isopycnals are shared between the channel and the NH, $\Delta b = 0$. In both sets of experiments (blue and black lines in Fig. 7b), $\Delta b \approx g\alpha(\Delta T + T_0)$, indicating that diffusivity plays a negligible role in determining the size of the isopycnal window.

The meridional width of the isopycnal window l_{win}, shown in Fig. 7, is the area between the outcrops of the

---

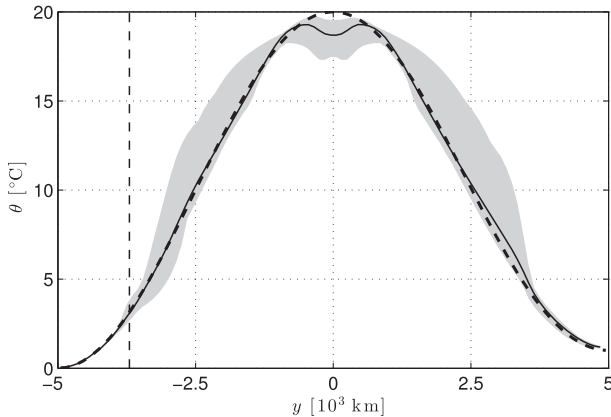[4] For a fixed value of κ_a, the variations of ψ with ΔT are nearly independent of the lat used to measure ψ.

FIG. 6. Zonal-mean surface temperature (solid line), $T^\star$ (dashed line), and the range of surface temperatures at each lat (shading) for the NO-SALT LOW-DIFF experiment with $\Delta T = 1.9°$C. The vertical dashed line shows the northern edge of the channel.

isopycnals $b = b_c$ and $b = \max(b_S, b_N)$, where b_S and b_N are the southernmost shared surface isopycnal; we set $l_{\text{win}} = 0$ if $\max(b_S, b_N) > b_c$. The variable l_{win} is highly constrained by $T^\star$, so

$$l_{\text{win}} \approx y_c - T^{\star-1}[T^\star(y_c) - \Delta T - T_0]$$

$$\approx \frac{L_y}{\pi}\left[1 - \sqrt{1 - \frac{4\sqrt{2}(\Delta T + T_0)}{T_{\text{eq}}}}\right], \quad (15)$$

where $T^{\star-1}$ is the inverse of $T^\star$ in the SH and $T^\star$ has been expanded to second order about $y_c = -3L_y/4$ to obtain the second line in (15). The approximation (15) is valid when l_{win} is positive and real; past the lower and upper ends of the region of validity, (15) is replaced with $l_{\text{win}} = 0$ and $l_{\text{win}} = L_y/\pi$, respectively. The variable l_{win} and (15) are compared in Fig. 8b; (15) provides a good approximation to l_{win} for $|\Delta T| < 1°$C but diverges slightly for $\Delta T > 1°$C.

A quantity that will be useful in scaling arguments later is h_c, the depth of the densest shared isopycnal; if there are no shared isopycnals, h_c is simply the depth of the lightest isopycnal to outcrop in the channel. The weak stratification at the base of the shared layer makes it difficult to determine the depth of the last shared isopycnal accurately, so, in practice, h_c is defined as the depth of an isopycnal slightly less dense than the densest shared isopycnal but still in the shared range. More precisely, h_c is the depth the isopycnal $b = \min[b_c, \max(b_S, b_N)] + (1/2)\Delta b$ averaged over the region of the tropics ($|y| < 500$ km) at least 100 km from the eastern or western boundary. This definition is similar to that of Nikurashin and Vallis (2012), who used the depth of a shared isopycnal averaged over a similar region. The

variation of h_c with ΔT is complex (Fig. 7d). The variable h_c generally peaks at 400–500 m near $\Delta T = -0.75°$C and decreases monotonically as ΔT is increased.

The behavior of $\psi_{\max}$ and h_c is simpler when plotted as a function of Δb instead of ΔT because the cases with $\Delta b < 0$ are excluded. As a function of Δb, $\psi_{\max}$ increases monotonically from 0 at $\Delta b = 0$. For $\Delta b > 1.5 \times 10^{-3}$ m s^{-2}, $\psi_{\max}$ is greater in the MOD-DIFF case than in the LOW-DIFF case, with the difference increasing with increasing Δb. In both the MOD-DIFF and LOW-DIFF cases, h_c increases to a maximum at $\Delta b \approx 10^{-3}$ m s^{-2} and decreases thereafter. The value h_c is systematically 100 m deeper in the MOD-DIFF case than in the LOW-DIFF case.

5. SALT results

a. Case study

As in section 4, we describe a specific case in detail before proceeding to examine the effects of varying ΔT. We will focus on the LOW-DIFF case, because the difference from the MOD-DIFF case is similar in both the SALT and NO-SALT experiments. These experiments are identical to those described in the LOW-DIFF NO-SALT case (i.e., $T_N^\star = 1°$C, so $\Delta T = 1.9°$C), except that freshwater forcing is turned on. The initial conditions for each SALT experiment were taken from the equilibrium conditions of the equivalent NO-SALT experiment.

The overturning circulation and stratification for the SALT case are shown in Fig. 9a. Compared to the NO-SALT cases, the overturning circulation is stronger and occupies a larger depth, buoyancy, and latitude range, and penetrates further into the channel (cf. Fig. 5b). The peak cross-equatorial transport is about 2.2 Sv—roughly 11% stronger than in the NO-SALT case. The increase in overturning is stronger for smaller ΔT—for $\Delta T = 0.9°$C, the overturning is 47% stronger in the SALT case than in the NO-SALT case. The isopycnals $2.3 \times 10^{-3} \leq b \leq 11.5 \times 10^{-3}$ m s^{-2} are shared between the NH and the channel; this range is almost twice as large as the equivalent NO-SALT experiment.

The abysssal water is lighter and less stratified in the SALT cases due to the heating and slight freshening of the deep isopycnals. The salt distribution (Fig. 9b) is asymmetric even though the salinity forcing is hemispherically symmetric. The NH is significantly saltier than the SH due to the salt transport from the northern subtropics (a region of net evaporation) into the northern subpolar region by the return branch of the overturning circulation (with a possible contribution from the wind-driven gyres). The overturning circulation acts
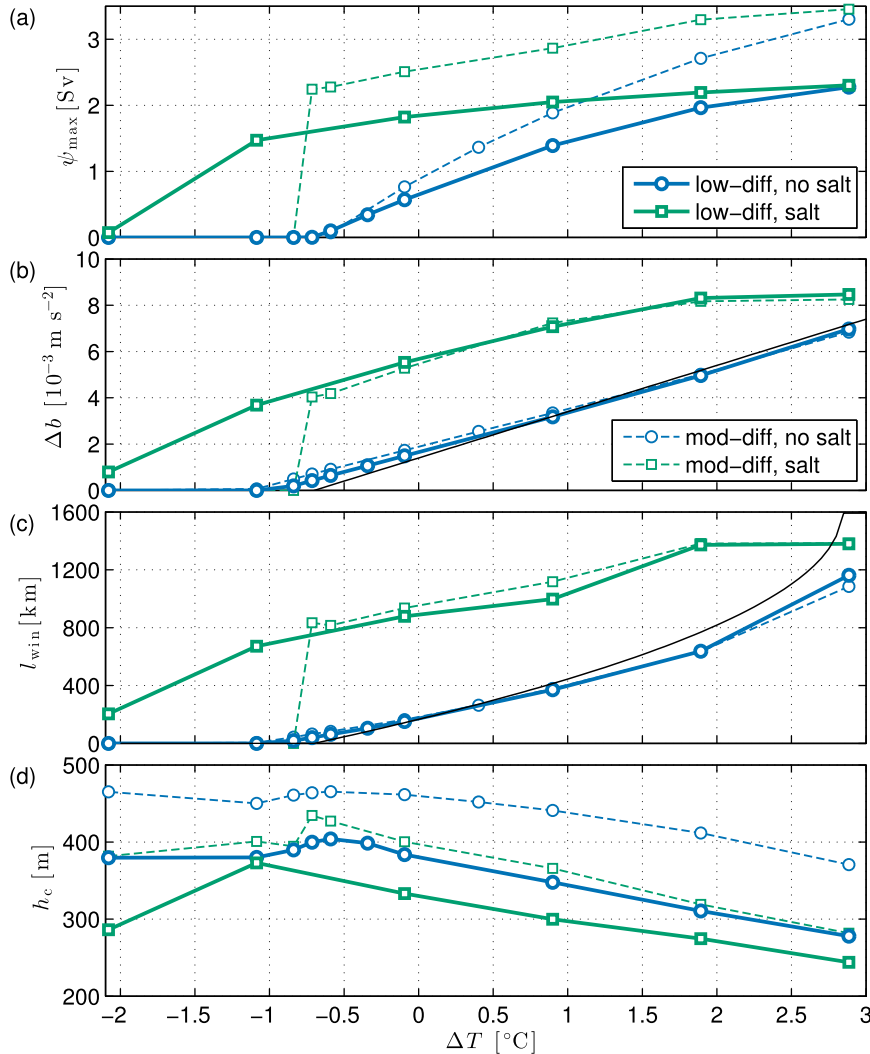
FIG. 7. (a) Max of the overturning streamfunction at the equator $\psi_{\max}$, (b) range of shared isopycnals Δb, (c) isopycnal window width l_{win}, and (d) depth of the deepest shared isopycnal h_c as a function of ΔT. The experiments with and without salt forcing are plotted using green squares and blue circles, respectively, while the solid and dashed lines give the low- and moderate-diffusivity cases, respectively. The thin black line in (b) gives l_{win} estimated using (15).

in the opposite sense in the SH, transporting freshwater from the channel north into the southern subtropics. The channel's only source of salty water is the upwelling of deep water formed in the NSG.

The strengthening of the overturning circulation under salinity forcing can be explained by the salt–advection feedback, which increases the buoyancy range of shared isopycnals: the northward advection of salt in the NSG mitigates the freshening due to the surface flux in this region relative to the SH channel region. At the same time, the freshwater carried by the upwelling branch of the overturning in the SH compounds the freshening effect of the local freshwater flux, leading to lower salinity in the channel water relative to the NSG.

Both these processes act to widen the range of buoyancy shared between the NSG and the SH channel; this further increases the overturning circulation. This process is illustrated in Fig. 10, which shows the surface buoyancy, and its thermal and haline components for one of the experiments shown in Fig. 9. The temperature distribution is essentially the same in the SALT and NO-SALT experiments, so the difference in the surface buoyancy distribution is due almost entirely to the presence of salt. The magnitude of the haline component of the buoyancy is small and only affects the subpolar regions where the thermal component is also small; these regions are, however, disproportionally important to the overturning circulation. Salinity forcing freshens
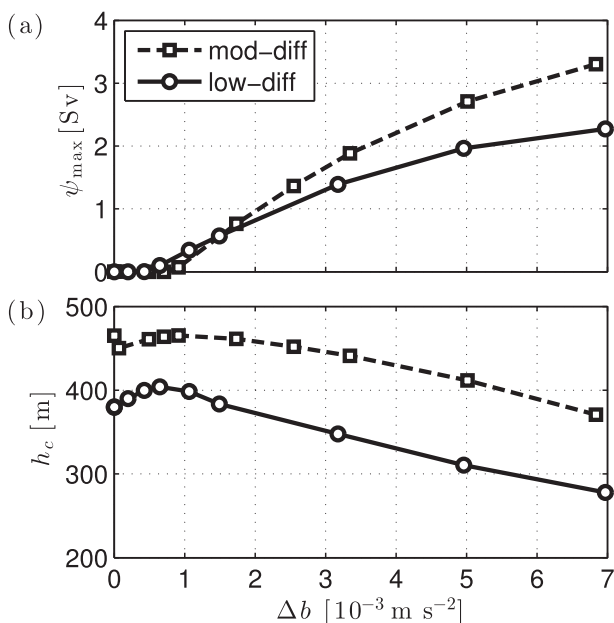
FIG. 8. (a) Max of the overturning streamfunction at the equator $\psi_{\max}$ [cf. (8)] and (b) depth of the deepest shared isopycnal h_c as function of Δb for the NO-SALT cases. Thick solid and dashed lines give the LOW-DIFF and MOD-DIFF cases, respectively.

both subpolar regions, but the salt–advection feedback limits the extent to which the northern subpolar region freshens, and increases the extent to which the SH channel freshens. The net effect is to increase the range of the shared isopycnals from 5.0×10^{-3} in the NO-SALT case to 9.1×10^{-3} m s^{-2} in the SALT case. In order for the salinity feedback to operate in the quasi-adiabatic setting, a temperature difference must exist between the meridional end points of the overturning cell. If the NH and the SH channel share all the surface temperature values, then the window of shared buoyancy is already at its maximum extent, and the haline component does not increase the overturning, as illustrated in Fig. 7 for the highest range of ΔT (green solid line in the range $\Delta T > 2°$C).

The salt feedback described above is quite different from the classical mechanism in the diffusive models described by Stommel (1961). In the diffusive case, the overturning transport is proportional to the difference in density between the downward and upward end points of the cell, and the salt feedback increases this density difference. In the quasi-adiabatic case, the overturning transports salt in such a way as to increase the shared surface buoyancy between the high-latitude end points of the cell and thus decreases the density differences between the upward and downward branch of the flow. In both the adiabatic and diffusive cases, the salinity feedback operates in the presence of a temperature gradient;

in this sense it is a thermohaline process, although the haline component has been stressed in the literature.

b. Variable ΔT

Figures 11a and 11b show b_S, b_c, and b_N in the NO-SALT experiments for moderate and low diffusivity, respectively. The surface buoyancies are strongly constrained by $T^\star$ and so both b_S and b_c are nearly constant, while b_N is linearly proportional to ΔT. For $\Delta T > 0$, the SALT cases also have b_S and b_c nearly constant, but offset from the NO-SALT values by about 4×10^{-3} m s^{-2} (Figs. 11c,d). Because the thermal components of the surface buoyancies are essentially unchanged for $\Delta T > 0$, this offset is due to a freshening of SH waters (cf. Fig. 9b). The density gradient across the channel $b_c - b_S$ is nearly the same in all cases. The variable b_N is dominated by the thermal component for $\Delta T > 0$ and so is similar in both the SALT and NO-SALT cases. In the SALT cases, $b_N < b_S$ for large ΔT, and the densest water is formed in the NH rather than the SH.

The behavior of the MOD-DIFF SALT and MOD-DIFF NO-SALT cases is markedly different for $\Delta T < 0$. The SALT case exhibits threshold-like behavior near $\Delta T \approx -0.75°$C; below this value, b_N suddenly increases and b_c suddenly decreases so that $b_N > b_c$ and the shared isopycnal window vanishes. This is accompanied by a reversal in the salt asymmetry; the NSG is now fresher than the channel. Similar threshold-like behavior is not apparent in the LOW-DIFF case, but cannot be ruled out without more experiments near $\Delta b \to 0$.

In general, the overturning circulation is stronger in the SALT than the NO-SALT cases (Fig. 7a). The term $\psi_{\max}$ also decreases more slowly as ΔT decreases in the SALT experiments than in the NO-SALT experiments. The MOD-DIFF experiments generally have larger $\psi_{\max}$ than the low-diffusivity experiments, except for $\Delta T < -1°$C, where the pole-to-pole component of the overturning circulation collapses in all cases except for the LOW-DIFF SALT case.

The increased $\psi_{\max}$ in the SALT cases is due to the salt–advection feedback freshening the Southern Ocean more than the NH, leading to an increase in the range of buoyancy values Δb shared between the channel and the NH (Fig. 7b). Remarkably, Δb increases by a nearly constant amount (approximately 4×10^{-3} m s^{-2}) over a wide range of ΔT. The constant offset relationship breaks down when ΔT is either very large (the densest water is formed in the NH) or very small (the overturning collapses). The MOD-DIFF and LOW-DIFF cases have essentially identical values of Δb so long as $\psi_{\max} > 0$, indicating that the interior diffusivity has little impact on the salt–advection feedback.
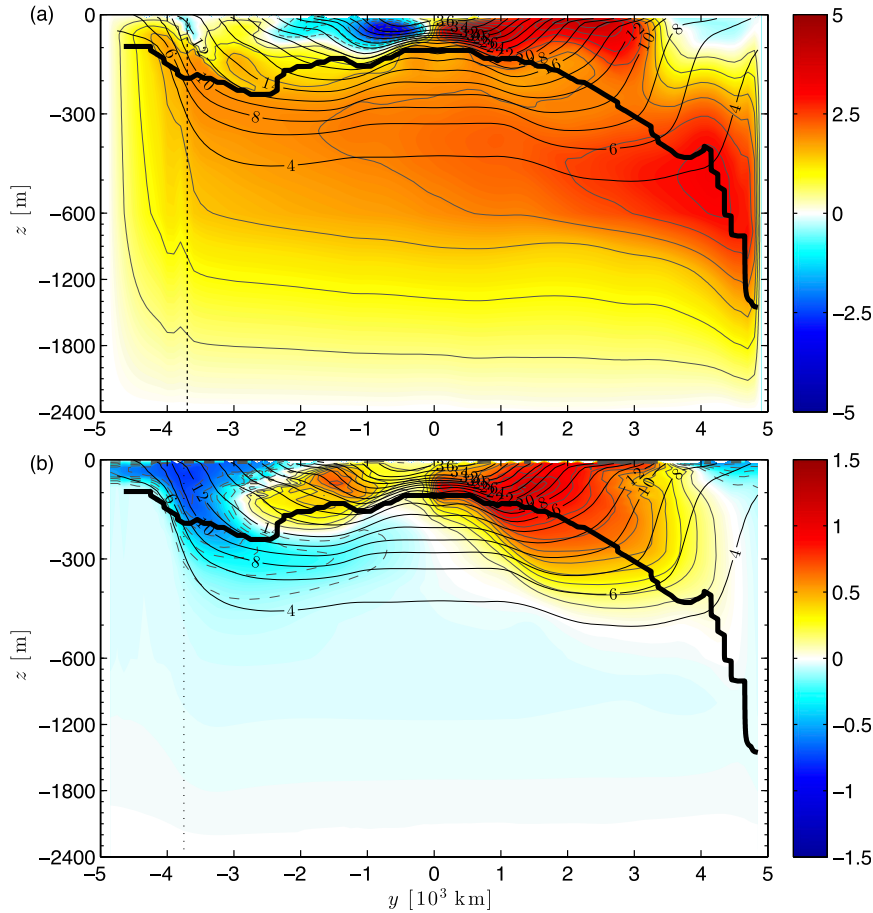
FIG. 9. (a) Overturning streamfunction ψ (colors and gray lines; interval is 0.25 Sv) and modified buoyancy $b^{\sharp}$ (black lines; $10^{-3}\,\mathrm{m\,s^{-2}}$) for the LOW-DIFF SALT case with $\Delta T = 1.9°C$. The thick black line gives an estimate of the base of the mixed layer. The northern edge of the channel is denoted by a vertical dashed line. (b) The TWA salinity anomaly (from $S_0 = 35$ psu) $\hat{S} - S_0$ (colors) for the experiment shown in (a). The lines in (b) have the same meaning as in (a).

The value of l_{win} increases monotonically with ΔT in the SALT experiments, but not in the same manner as in the NO-SALT experiments (Fig. 7c). In the SALT experiments, l_{win} is about 600 km wider in the SALT experiments than in the NO-SALT experiments for intermediate values of ΔT and fills the entire channel for $\Delta T > 2°C$. Note that the maximum value of $l_{\mathrm{win}} \approx$ 1400 km, which is greater than the 1250 km width of the channel. This is possible because the outcrop of the $b = b_c$ isopycnal overshoots y_c northward, following streamlines, downstream of the tip of the model's "South America," much like the Malvinas Current in the South Atlantic Ocean. As discussed in Allison et al. (2010), the northernmost zonally reentrant streamline marks the dynamical northern edge of the channel; generally the dynamical edge of the channel is to the north of its geographical edge.

The variation of h_c with ΔT is similar to that of the NO-SALT experiments—h_c peaks in the range $-1° < \Delta T < 0°C$ and then decreases as ΔT increases further. As with the NO-SALT experiments, h_c is greater in the MOD-DIFF experiments than in the LOW-DIFF cases.

The behavior of ψ_{max}, l_{win}, and h_c as a function of Δb is shown in Fig. 12. As in the NO-SALT cases, ψ_{max} increases monotonically with Δb, but h_c peaks at an intermediate value of Δb and decays for both larger and smaller Δb. There are few data points for $\Delta b < 4 \times 10^{-3}\,\mathrm{m\,s^{-2}}$ due to the action of the salt–advection feedback—the system tends to move away from the point $\Delta b = 0$ while $\Delta b > 0$ by freshening the channel.

c. The relationship between Δb and ΔT

Figure 7b shows that $\Delta b \approx g\alpha\Delta T + b_0$, where b_0 is an approximately constant offset that is independent of
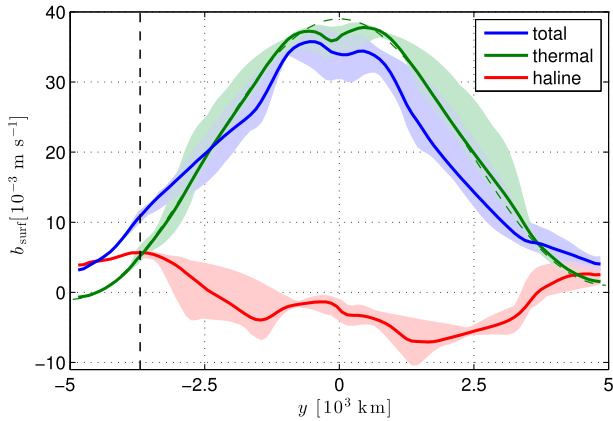
FIG. 10. Zonal-mean surface buoyancy b_{surf} and its thermal and haline components (solid lines) as a function of lat y for the LOW-DIFF SALT case with $\Delta T = 1.9°C$. The shading gives the envelope of each component as a function y. The surface relaxation profile $g\alpha(T^\star - \theta_{ref})$ is given by a green dashed line for reference.

diffusivity. In this section, we show that the value of b_0 is a consequence of the salt balance in the channel. First, we note that the surface temperature distribution is nearly identical in the SALT and NO-SALT cases, so the isotherm outcrops may be regarded as fixed. Thus, the problem of finding b_0 reduces to finding the surface salinity distribution. Second, the circulation in the NH tends to cause freshwater to accumulate in the western half of the basin, while the deep water (i.e., the densest

water formed in the NH) is formed in the northeastern corner of the domain (Fig. 13), which receives the salinity of the model's North Atlantic Current, created at the boundary of the SPG and the subtropical gyre, with zero salinity anomaly. Because the deep water flows quasi adiabatically, it retains its salinity anomaly so the deep-water upwelling in the channel has the salinity of the northernmost shared outcrop S_N, until it enters the channel (cf. the TWA salinity shown in Fig. 9b).

The zonally averaged salinity budget in the channel is

$$(v^\dagger \overline{S})_y + (w^\dagger \overline{S})_z = (\kappa_v \overline{S}_z)_z + \nabla \cdot \overline{K_{Redi} \nabla S}, \quad (16)$$

where the residual velocity is $\mathbf{u}^\dagger \equiv \overline{\mathbf{u}} + \mathbf{u}^\star$. The barred velocities are the zonally averaged "resolved" velocities, the starred velocities are due to the GM parameterization, and $\mathbf{K}_{Redi}$ is the Redi (1982) tensor.

The Redi component can be estimated by considering that $\mathbf{K}_{Redi}$ tapers to horizontal diffusion with diffusivity κ_e in the mixed layer, so that

$$\nabla \cdot \overline{K_{Redi} \nabla S} \sim \frac{\kappa_e S_h}{L^2}, \quad (17)$$

where S_h is a scale for horizontal variations in salinity and L is a typical length scale. This should be compared to the magnitude of the advective terms, which we estimate as
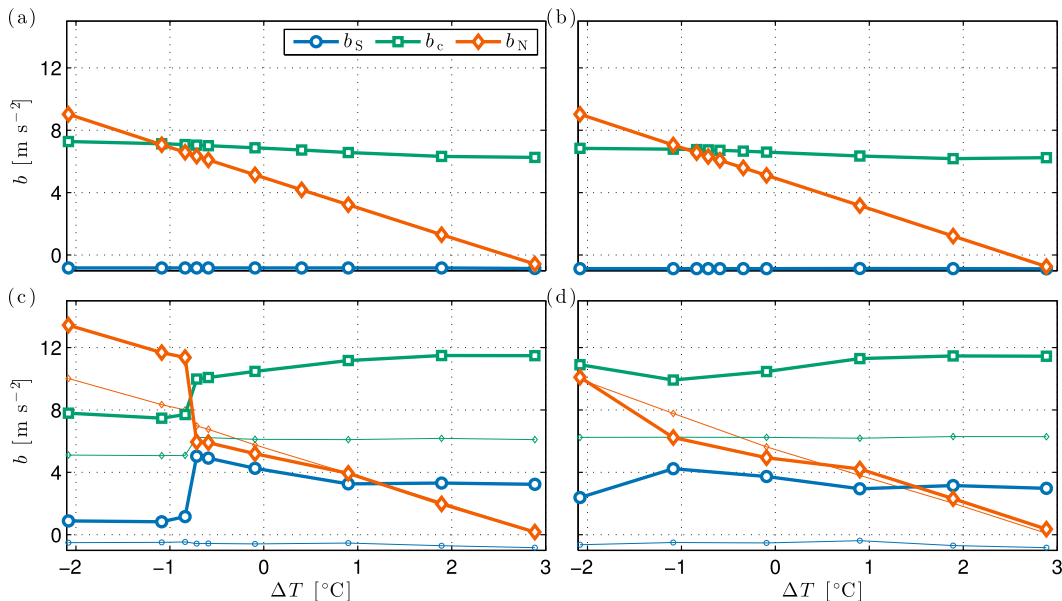

FIG. 11. Min buoyancy in the SH and NH, b_S (blue circles) and b_N (orange diamonds), respectively, and max buoyancy in the channel b_c (green squares) as a function of the range of shared temperatures ΔT imposed by the surface forcing for the four cases: (a) NO-SALT MOD-DIFF, (b) NO-SALT LOW-DIFF, (c) SALT MOD-DIFF, and (d) SALT LOW-DIFF. The thermal components of the surface buoyancies are also given in (c) and (d) by thin lines and small symbols.
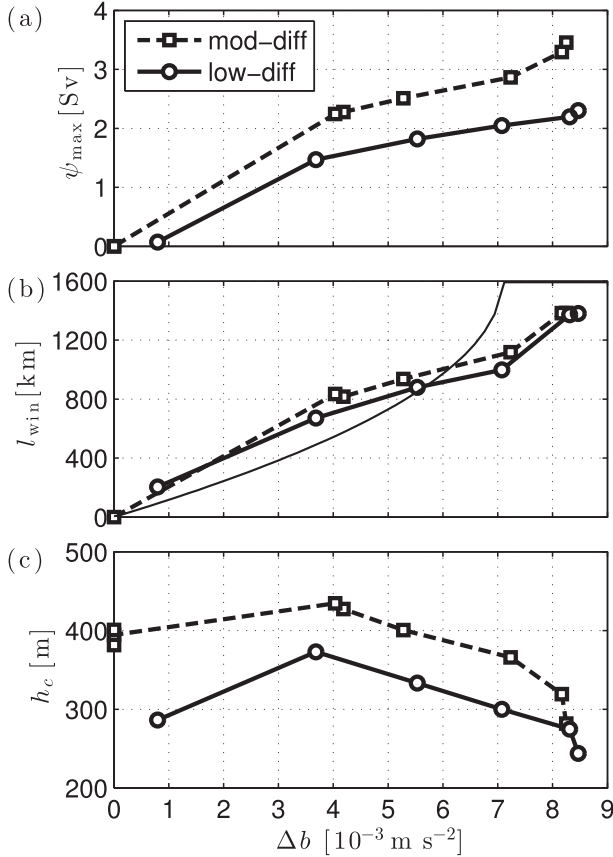
FIG. 12. (a) Max of the overturning streamfunction at the equator $\psi_{\max}$, (b) width of the isopycnal window in the channel l_{win}, and (c) depth of the deepest shared isopycnal h_c as a function of isopycnal window width Δb for the NO-SALT cases. Thick solid and dashed lines give the LOW-DIFF and MOD-DIFF cases, respectively. The thin line in (b) gives the estimate of l_{win} from (30).

$$(v^{\dagger}\overline{S})_y \sim \frac{v_{\text{Ek}}S_h}{L}, \tag{18}$$

where

$$v_{\text{Ek}} \sim \frac{\tau}{\rho f d} \tag{19}$$

is the velocity in the surface Ekman layer and d is the thickness of the mixed layer as defined in (2). Appropriate scales for the channel are $L \sim 1000\,\text{km}$, $\tau \sim 0.1\,\text{Pa}$, $f = 10^{-4}\,\text{s}^{-1}$, and $d = 40\,\text{m}$. The salinity distribution in the channel is remarkably uniform, with $S_h \sim 0.2\,\text{psu}$. Using these scales, the ratio of the Redi term to the advective term is $\sim 1.5 \times 10^{-2}$. The Redi term is required to satisfy the boundary condition $S_y = 0$ at $y = L_y$, where it provides a correction to the derivative of S at $y = L_y$ and a negligible contribution to the value of S. Thus, the Redi term can safely be ignored away from the southern boundary.

The near-surface balance without the Redi term is

$$(v^{\dagger}\overline{S})_y + (w^{\dagger}\overline{S})_z = (\kappa_v \overline{S}_z)_z. \tag{20}$$

Integrating from a depth $-D$, where $\kappa_v \overline{S}_z \approx 0$, to the surface gives

$$\frac{\partial}{\partial y} \int_{-D}^{0} v^{\dagger}\overline{S}\,dz - w^{\dagger}(-D)S_N = \mathcal{F}, \tag{21}$$

where $\mathcal{F}$ is the surface salt flux defined in (6); we have used the assumption that $S \approx S_N$ beneath the surface layer. The region $z > -D$ encompasses, but is slightly thicker than, the mixed layer. Becausee S is constant throughout most of this region, we replace $\overline{S}$ with its surface value S_0 in (21), finding

$$\frac{\partial}{\partial y} S_0 V^{\dagger} - \overline{w}(-D)S_N = \mathcal{F}, \tag{22}$$

where

$$V^{\dagger} \equiv \int_{-D}^{0} v^{\dagger}\,dz. \tag{23}$$

Noting that $w^{\dagger}(-D) = \partial_y V^{\dagger}$, the surface layer budget (22) then becomes the simple differential equation

$$(V^{\dagger}S_0)_y = S_N V_y^{\dagger} + \mathcal{F}. \tag{24}$$

We now integrate (24) over the width of the channel, to obtain

$$S_S = S_N + \frac{E_s}{V^{\dagger}(y_c)}, \tag{25}$$

where we have denoted with $S_S \equiv S_0(y_c)$ the surface salinity at $y = y_c$, $E_s \equiv \int_{-L_y}^{y_c} \mathcal{F}\,dy$ is the surface salt flux integrated over the meridional extent of the channel, and we have used the no-normal flow condition $V^{\dagger}(-L_y) = 0$. Thus, this expression gives the difference between the salinity at the northernmost shared outcrop and the salinity of the northern edge of the channel, as long as there is a pole-to-pole overturning circulation that carries S_N southward.

To proceed, we need an expression for $V^{\dagger}(y_c)$. A reasonable assumption is that $V^{\dagger}(y_c)$ is proportional to the residual transport at the equator $V_{\max}^{\dagger} \equiv \psi_{\max}/L_x$; however, we will show that $V^{\dagger}(y_c)$ is better approximated by the Ekman transport $V_{\text{Ek}} \equiv -\tau/(\rho f)$ at y_c. In the channel, the residual streamfunction is the sum of V_{Ek} and the transport associated with the eddy parameterization V_{GM}. Because the vertical scale of V_{GM} is much larger than the mixed-layer depth d, the net
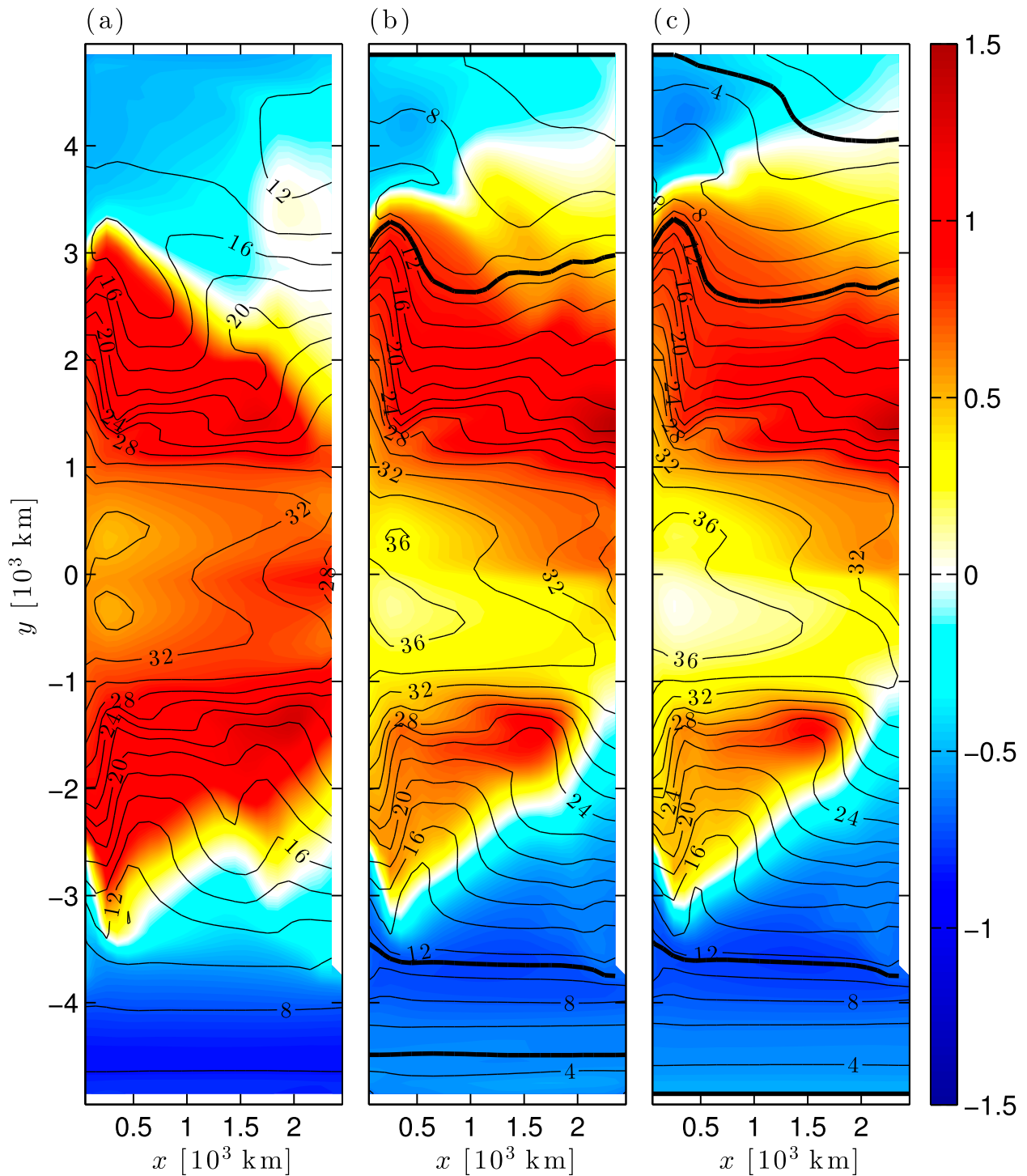
FIG. 13. Surface salinity anomaly (colors; psu) and surface buoyancy (contours; $10^{-3}\,\mathrm{m\,s^{-2}}$) for LOW-DIFF SALT experiments with (a) $\Delta T = -2.1°$, (b) $\Delta T = 0.1°$, and (c) $\Delta T = 2.9°C$. The thick dark lines show the boundaries of the shared isopycnals.

transport in the mixed layer is approximately $V^{\dagger}(y_c) \approx V_{\mathrm{Ek}} + dv_{\mathrm{GM}}$. For the thin value of the mixed layer used here, the eddy transport is negligible compared to the Ekman transport and we have

$$V^{\dagger} \approx V_{\mathrm{Ek}} = -\frac{\tau}{\rho f}. \qquad (26)$$

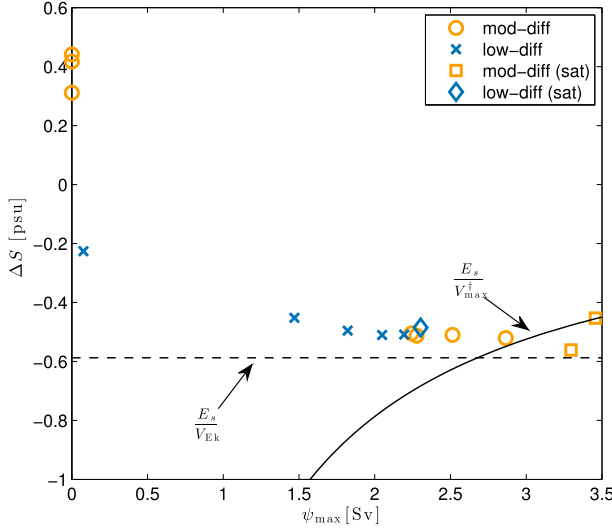We thus find that the difference $\Delta S \equiv S_N - S_S$ is given by

FIG. 14. The difference, $\Delta S = S_S - S_N$, between the TWA salinities averaged in x and y over the mixed layer at constant buoyancy along the southern outcrop of the isopycnal $b = b_c$; S_S and the northern outcrop of the isopycnal $b = \max(b_S, b_S) S_N$ as a function of $\psi_{\max}$. The dashed line gives (27), and the solid line gives $E_s / V^{\dagger}_{\max}$. The square and diamond symbols indicate saturated states, where the bottom water is formed in the NH rather than in the channel.

$$\Delta S = \frac{E_s}{V_{\text{Ek}}}. \tag{27}$$

Figure 14 compares the prediction in (27) (dashed line) with the values of ΔS obtained in the model for different values of the parameters. For comparison, the prediction obtained by replacing V_{Ek} with $V^{\dagger}_{\max}$ is also shown (solid line). The essential point is that when $\psi_{\max} = 0$, there is no connection between the salinities in the channel and in the NH, leading to a reversed sign of the surface salinity gradient in the channel region (cf. the points with positive ΔS in Fig. 14).

The value predicted by (27) is 34.4 psu. The buoyancy anomaly associated with this salinity anomaly is $4.4 \times 10^{-3} \, \text{m s}^{-2}$, approximately the size of the Δb offset between the SALT and NO-SALT experiments.

6. Scaling

The results of sections 4 and 5 can be interpreted using a modification of the scaling law first introduced by Gnanadesikan (1999). This scaling law is derived by equating expressions for the strength of the overturning circulation due to geostrophically balanced overturning in the NSG Ψ_n, diffusive upwelling the tropics and subtropics Ψ_d, and wind- and eddy-driven overturning in the channel Ψ_w and Ψ_e, respectively, and takes the form of a cubic equation for h_c:

$$\underbrace{\frac{\Delta b h_c^2}{f_N}}_{\Psi_n} + \underbrace{\frac{\kappa_e h_c L_x}{l_{\text{win}}}}_{\Psi_e} = \underbrace{\frac{\tau_0 L_x}{\rho f_S}}_{\Psi_w} + \underbrace{\frac{\kappa_a L_x L_b}{h_c}}_{\Psi_d}. \tag{28}$$

We follow Nikurashin and Vallis (2012) when interpreting the terms in (28): Δb is the range of isopycnals shared between the channel and the Northern Hemisphere, h_c is the depth of the densest shared isopycnal, l_{win} is the meridional extent of the shared isopycnals in the channel, τ_0 is a representative wind stress over the channel, L_b is the meridional extent of the tropics and subtropics, and f_S and f_N are scales for the Coriolis parameter in the channel and the NSG, respectively. Note that all parameters appearing in (28) are defined to be positive. The values of κ_e, κ_a, and L_x are given in section 2. For the other parameters, we use $f_N = f_S = 10^{-4} \, \text{s}^{-1}$, $\tau_0 = 0.1 \, \text{Pa}$, $\rho = 1000 \, \text{kg m}^{-3}$, and $L_b = 8000 \, \text{km}$. In practice, Δb and h_c are as defined in section 4b.

The quantity we wish to predict using (28) is $\psi_{\max}$, the maximum value of the streamfunction at the equator. Because the tropics and subtropics—where diffusive upwelling makes its largest contribution—are symmetrically distributed about the equator, $\psi_{\max}$ will be equal to Ψ_n minus half the diffusive loss in the tropics and subtropics; that is,

$$\psi_{\max} \sim \Psi_n - \frac{1}{2} \Psi_d = \frac{\Delta b h_c^2}{f_N} - \frac{\kappa_v L_x L_b}{2 h_c}. \tag{29}$$

a. Determination of l_{win}

We have seen that l_{win} varies with Δb (cf. Fig. 7c). In the NO-SALT cases, both Δb and l_{win} are approximately fixed by $T^{\star}$, allowing us to rewrite (15) in terms of Δb:

$$l_{\text{win}} \approx \frac{L_y}{\pi} \left(1 - \sqrt{1 - \frac{4\sqrt{2} \Delta b}{\alpha_\theta g T_{\text{eq}}}} \right). \tag{30}$$

In the SALT cases, the surface buoyancy is not constrained by $T^{\star}$, and the position of the shared isopycnals is part of the solution, while in (30) we have assumed the same approximate functional form as in the NO-SALT case. A more complete theory would have to incorporate the prediction of the position of the shared surface isopycnals; this is part of ongoing work. Understandably, the fit is not as good as for the NO-SALT cases (cf. Figs. 7c, 12).

Note that both Gnanadesikan (1999) and Nikurashin and Vallis (2012) assume that l_{win} is fixed and (approximately) equal to the width of the channel. Neither of these studies considered variations in Δb, so they did not

need to specify any functional relationship between l_{win} and Δb. The present scaling is equivalent to those used by Gnanadesikan (1999) and Nikurashin and Vallis (2012) for large Δb, because $l_{\text{win}} = L_y + y_c$ for $\Delta b \gtrsim 8 \times 10^{-3}\,\text{m s}^{-2}$; however, differences are apparent for smaller Δb.

b. Nondimensionalization

To ease direct comparison with other studies, we nondimensionalize (28) by setting $h_c = H_0 h$ and $l_{\text{win}} = l_c l$, where H is a scale for the depth of the overturning circulation and l_c is the width of the channel. For simplicity, we also assume $f_S \sim f_N \sim f_0$. After division by $\tau_0 L_x/(\rho f_0)$, (28) assumes the nondimensional form

$$\frac{\text{Ro}}{\text{Fr}} h^2 + \frac{\text{Ek}_h}{\sigma_h \text{Ro}} \frac{L_x}{l_c} \frac{h}{l} = 1 + \frac{\text{Ek}_v}{\sigma_v \text{Ro}} \frac{L_x L_b}{l_c^2} \frac{1}{h}, \quad (31)$$

where

$$\text{Ro} \equiv \frac{U}{f_0 L_x}, \quad \text{Fr} \equiv \frac{U^2}{\Delta b H_0}, \quad (32)$$

$$\frac{\text{Ek}_h}{\sigma_h} \equiv \frac{\kappa_e}{f_0 L_x^2}, \quad \text{and} \quad \frac{\text{Ek}_v}{\sigma_v} \equiv \frac{\kappa_a}{f_0 H^2} \quad (33)$$

are the Rossby number, the Froude number, the quotient of the horizontal Ekman and Prandtl numbers, and the quotient of the vertical Ekman and Prandtl numbers, respectively. The velocity scale

$$U \equiv \frac{\tau_0}{\rho f_0 H_0} \quad (34)$$

is determined by the wind.

The depth scale H_0 is not the full depth of the basin, but rather a characteristic value of h; we pick $H_0 = 160\,\text{m}$, which is obtained by requiring that $\text{Ro} \sim \text{Fr}$ for $\Delta b = 10^{-2}\,\text{m s}^{-2}$. The other parameters are given at the beginning of this section. The values of the groups of nondimensional parameters appearing in (31) are

$$\frac{\text{Ro}}{\text{Fr}} = 0 - 1.0, \quad (35)$$

$$\frac{\text{Ek}_h}{\sigma_h \text{Ro}} \frac{L_x}{l_c} = 0.063, \quad \text{and} \quad (36)$$

$$\frac{\text{Ek}_v}{\sigma_v \text{Ro}} \frac{L_x L_b}{l_c^2} = 0.63 - 5.0. \quad (37)$$

The ranges in (35) and (37) are due to variations in Δb and κ_a. Despite the difference in domain size, the magnitudes of these terms differ from those used by
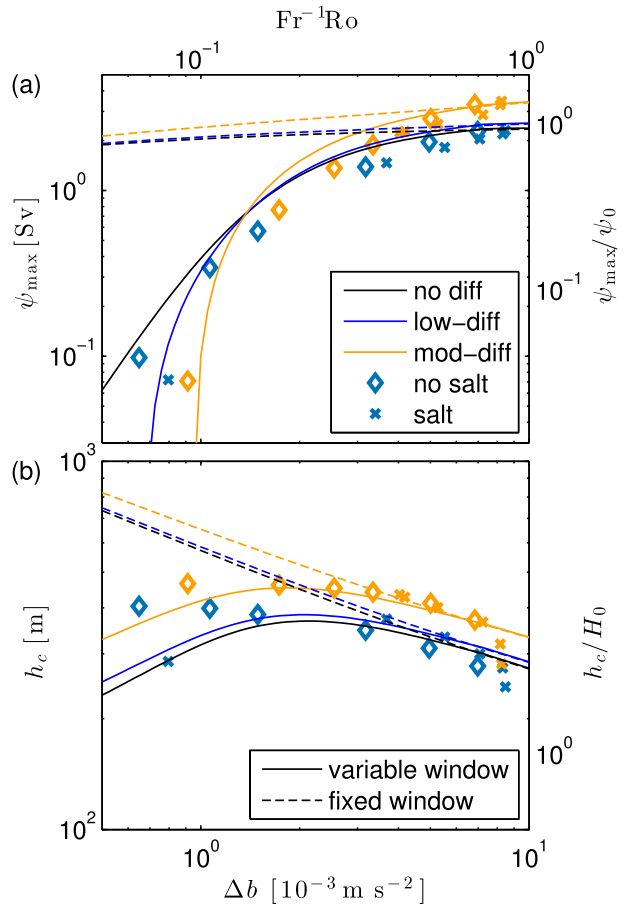

FIG. 15. The (a) ψ_{max} and (b) h_c as a function of Δb (equivalently, Ro/Fr) for the NO-SALT MOD-DIFF (orange diamonds), NO-SALT LOW-DIFF (blue diamonds), SALT MOD-DIFF (orange crosses), and SALT LOW-DIFF (blue crosses) experiments. Nondimensional values are given on the right axes. The solid and dashed lines give solutions to (28) with variable and fixed l_{win}, respectively. The colors of the lines indicate the value of κ_a used in (28): black, blue, and orange for $\kappa_a = 0$, $\kappa_a = 3.125 \times 10^{-6}$, and $\kappa_a = 2.5 \times 10^{-5}\,\text{m}^2\,\text{s}^{-1}$, respectively. The solid curves in (b) have been shifted upward by 120 m to account for the mixed layer and ventilated thermocline that are ignored in (28).

Gnanadesikan (1999) and Nikurashin and Vallis (2012) by less than 20%, except for the diffusive term, which is one order of magnitude larger in Gnanadesikan (1999) than here or in Nikurashin and Vallis (2012). For comparison to Gnanadesikan (1999) and Nikurashin and Vallis (2012), we used $H_0 = 320\,\text{m}$ and $H_0 = 800\,\text{m}$, respectively.

c. Comparison to model results

Figure 15 shows ψ_{max} and h_c as a function of Δb [equivalent of $(\text{Fr}^{-1})\text{Ro}$] for all of the experiments. Nondimensional scales are given on the top and right axes, respectively, of each panel; ψ_{max} is nondimensionalized by $\psi_0 = 2.5\,\text{Sv}$, which is the value of Ψ_n for $h_c = H_0$ and

$\Delta b = 10^{-2}\,\mathrm{m\,s^{-2}}$. For comparison, solutions to (28) for fixed and variable l_{win} and three diffusivities are also shown. As expected, the solutions with l_{win} fixed and variable are identical for "large" Δb (i.e., $\mathrm{Fr}^{-1}\,\mathrm{Ro} > 0.6$), but differences are apparent for smaller Δb. While both sets of solutions for $\psi_{\max}$ tend toward 0 as $\Delta b \to 0$, solutions with variable l_{win} decay more quickly. The variable l_{win} solutions for h_c display nonmonotonic behavior, peaking near $\mathrm{Fr}^{-1}\,\mathrm{Ro} = 0.2$ and tending toward zero for both small and large Δb. In contrast, the solutions with fixed l_{win} decrease monotonically.

The nondiffusive solutions (i.e., $\kappa_a = 0$; black lines) are only slightly offset from the LOW-DIFF curve for $\mathrm{Fr}^{-1}\,\mathrm{Ro} > 0.1$, indicating that the LOW-DIFF experiments are indeed close to the adiabatic limit. For $\mathrm{Fr}^{-1}\,\mathrm{Ro} < 0.1$, diffusion becomes important and both sets of experiments diverge from the $\kappa_a = 0$ curve—diffusion favors the recirculating component over the pole-to-pole component of the overturning circulation, so $\psi_{\max}$ decays faster as $\Delta b \to 0$ for larger κ_a.

The overturning strengths diagnosed from the model follow the variable window curves more closely than the fixed window curves where the two can be distinguished ($\mathrm{Fr}^{-1}\,\mathrm{Ro} < 0.4$) (Fig. 15a). The model-diagnosed depths h_c also appear to agree better with variable window curves than the fixed window curves (Fig. 15b), although the agreement is not as clear as in Fig. 15a. These results demonstrate that the pole-to-pole component of the overturning circulation is indeed sensitive to the geographical width l_{win} as well as the size Δb of the isopycnal window.

7. The salt transport

One question that arises is how the pole-to-pole circulation achieves a salt balance while connecting two high-latitude regions where the freshwater flux is of the same sign. Considering a region bounded by two shared isopycnals, quasi adiabatic in the interior, the imposed freshwater flux does not typically integrate to zero in the area where isopycnals surface. Thus, a steady state can only be achieved if there is a considerable salt transport across the isopycnals, presumably in the surface diabatic layer.

The salt budget can be written as

$$S_t + \nabla \cdot \mathbf{F} = 0, \qquad (38)$$

where

$$\mathbf{F} \equiv \mathbf{u}^\dagger S - \mathbf{K}_{\mathrm{Redi}} \nabla S - \kappa_v S_z \hat{\mathbf{k}} \qquad (39)$$

and $\mathbf{u}^\dagger$ are the sum of the 3D resolved and parameterized velocities. The time and zonal TWA [defined in (12)] of the salt budget is

$$\iiint (\nabla \cdot \mathbf{F}) \delta(b - \tilde{b}) \, dz \, dx \, dt = 0, \qquad (40)$$

where we have suppressed the integration limits and assumed that the flow is statistically steady so that the tendency term vanishes. Using integration by parts to move the derivatives to the δ function, we find

$$\frac{\partial}{\partial y} \iiint \mathbf{j} \cdot \mathbf{F} \delta(b - \tilde{b}) \, dz \, dx \, dt$$
$$+ \frac{\partial}{\partial \tilde{b}} \iiint \nabla b \cdot \mathbf{F} \delta(b - \tilde{b}) \, dz \, dx \, dt$$
$$= \iint \mathcal{F}(S) \delta(b_0 - b) \, dx \, dt. \qquad (41)$$

Note that y derivatives are taken at constant $\tilde{b}$.

In analogy to the streamfunction (8), we define a "salt function"

$$\Sigma(y, \tilde{b}) \equiv \frac{1}{T} \iiint \mathbf{j} \cdot \mathbf{F} \mathcal{H}(b - \tilde{b}) \, dz \, dx \, dt, \qquad (42)$$

which satisfies

$$\Sigma_{\tilde{b}} = -\frac{1}{T} \iiint \mathbf{j} \cdot \mathbf{F} \delta(b - \tilde{b}) \, dz \, dx \, dt \quad \text{and} \qquad (43)$$

$$\Sigma_y = \frac{1}{T} \iiint \nabla b \cdot \mathbf{F} \delta(b - \tilde{b}) \, dz \, dx \, dt$$
$$- \frac{1}{T} \iint \mathcal{F}(S) \mathcal{H}(b_0 - \tilde{b}) \, dx \, dt. \qquad (44)$$

Much like the streamfunction, the salt function is constant on isopycnals (i.e., $\Sigma_y = 0$) for adiabatic flow. In the case of the salt function, diabatic effects arise either from diapycnal flux [first term in (44)] or flux across the sea surface [second term in (44)].

The term Σ is not uniquely defined; in particular, the modified salt function

$$\Sigma' = \Sigma + \int_{-\infty}^{\tilde{b}} \psi_{\tilde{b}} S^\star(\psi) \, db \qquad (45)$$

also satisfies (41) for any $S^\star$ that is a function of ψ only. This modification is equivalent to subtracting a spatially variable background salt field from S. The goal is to choose $S^\star$ in a manner that results in a physically meaningful salt function. Boccaletti et al. (2005) argue that, because only tracer values that vary on streamlines contribute to the net tracer flux, $S^\star$ should be the circulation-weighted salinity on streamlines; that is,
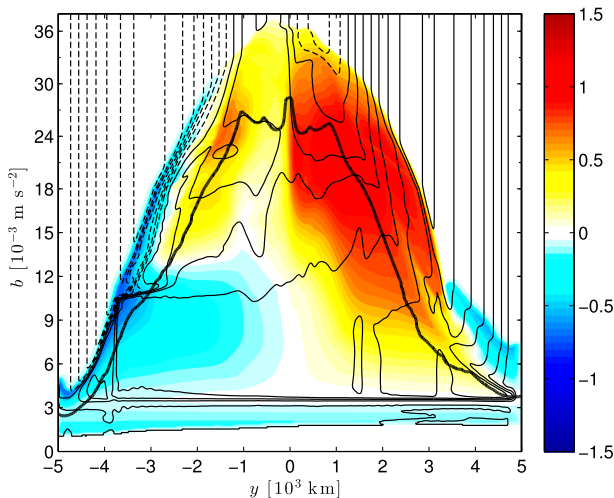
FIG. 16. The colors give the TWA salt anomaly from S_{ref}, and the contours give the freshwater function $-\Sigma/S_{ref}$ as a function of y and b. The contour intervals are 7.5×10^{-3} Sv. The buoyancy spacing is compressed above 18×10^{-3} m s^{-2} by a factor of 2.5. The minor ticks above 18×10^{-3} m s^{-2} are 3×10^{-3} m s^{-2} apart to match the major ticks below 18×10^{-3} m s^{-2}. The thick black line shows an estimate of the base of the mixed layer.

$$S^{\star}(\psi_0) = \frac{\oint |\nabla\psi| \hat{S} \, d\ell}{\oint |\nabla\psi| \, d\ell}, \qquad (46)$$

where $\hat{S}$ is the TWA salt field and the integrals are taken on the contours $\psi = \psi_0$. This choice of $S^{\star}$ eliminates the largest possible portion, in a least squared sense, of the advective salt flux (Boccaletti et al. 2005).

The freshwater function for a LOW-DIFF SALT case with $\Delta T = 0.9°$C, given by $-\Sigma/S_{ref}$, is contoured as a function of y and b in Fig. 16. It shows that the freshwater flux enters in the subpolar NH, circulates clockwise quasi isopycnally in a pole-to-pole cell all the way to the channel, where it upwells in the mixed layer to return quasi isopycnally in the subtropical NH, where the surface freshwater flux changes sign (black solid lines). Conversely, the cell in the SH is very shallow and connects directly in the mixed layer the region of positive freshwater flux in the SH to the region of negative freshwater flux within the same hemisphere (black dashed lines).

8. Summary and conclusions

We have shown that, if all other parameters are fixed, the strength of the pole-to-pole overturning circulation is controlled by the size of the shared isopycnal Δb, outcropping in both the reentrant channel and the Northern Hemisphere. If buoyancy is a function of temperature only, Δb can be specified by specifying the surface

temperature relaxation profile, because the rapid relaxation ensures that the surface temperature is nearly prescribed. Salt forcing is better represented by a fixed-flux condition, and this type of boundary condition decouples the surface buoyancy distribution from the surface forcing, so that Δb is no longer determined by prescribing the atmospheric state. We find that Δb in the SALT cases is shifted by a nearly constant offset compared to the NO-SALT cases; the magnitude of this offset is determined in the channel mixed layer and can be estimated by considering the salinity budget in this region.

In all cases, salt forcing leads to a stronger overturning circulation for a given surface temperature distribution. This is due to a salt–advection feedback in which near-surface salt from the subtropics is transported into the NH, partially counteracting the effect of excess precipitation. No such feedback occurs in the SH; precipitation over the channel increases the surface buoyancy, bringing more isopycnals into the range of those in the NH and increasing Δb. The freshening of the channel is halted by the upwelling of relatively salty deep water and the export of freshwater in the surface Ekman layer. The final value of the salinity is controlled by the salt budget in the channel, which depends on the local freshwater flux, the strength of the overturning circulation, and the value of the salinity in the NSG, which is upwelled in the channel; that is, it depends on both local and remote processes. The main effect of the salt feedback is to increase the surface buoyancy in the channel more than in the NSG, leading to a wider shared window and a stronger overturning.

The scaling theory of Gnanadesikan (1999), which predicts the strength of the pole-to-pole component of the overturning ψ_{max} and depth of the shared isopycnals h_c, is improved to account for variations of the meridional extent of the shared isopycnal window l_{win}.

The freshwater transport is visualized in buoyancy coordinates through a salt function that illustrates the connection between the NH subpolar region and the subtropics via the pole-to-pole circulation. Conversely, the freshwater transport in the SH is short circuited through a direct connection from the subpolar to the subtropical region confined to the mixed layer.

All the experiments discussed here have been run to an approximately steady state. The NO-SALT experiments converge to an absolutely steady state. The SALT experiments are weakly time dependent, with unsteadiness coming primarily in the form of intermittent convective adjustment in the NSG. These transient features are small in scale, have short time scales, and do not cause significant fluctuations in large-scale quantities such as Δb and ψ_{max}. However, the threshold behavior observed in the MOD-DIFF SALT cases suggests the existence of multiple equilibria in a nearby

part of the parameter space. Convergence to a unique steady state is not generic behavior for salt-forced circulations; large-scale thermohaline oscillations and multiple equilibria are commonly observed and we expect the unique steady states that we found to be destabilized by introducing asymmetries into the salt forcing (Stommel 1961; Bryan 1986; Cessi and Young 1992; Marotzke 2000). The resulting thermohaline oscillations and multiple equilibria will be examined in a forthcoming paper.

REFERENCES

Allison, L. C., H. L. Johnson, D. P. Marshall, and D. R. Munday, 2010: Where do winds drive the Antarctic Circumpolar Current? *Geophys. Res. Lett.,* **37,** L12605, doi:10.1029/2010GL043355.

Boccaletti, G., R. Ferrari, A. Adcroft, D. Ferreira, and J. Marshall, 2005: The vertical structure of ocean heat transport. *Geophys. Res. Lett.,* **32,** L10603, doi:10.1029/2005GL022474.

Bryan, F., 1986: High-latitude salinity effects and interhemispheric thermohaline circulations. *Nature,* **323,** 301–304, doi:10.1038/323301a0.

Bryden, H. L., and S. Imawaki, 2001: Ocean heat transport. *Ocean Circulation and Climate,* G. Siedler, J. Church, and J. Gould, Eds., Academic Press, 455–474.

Cessi, P., and W. R. Young, 1992: Multiple equilibria in two-dimensional thermohaline circulation. *J. Fluid Mech.,* **241,** 291–309, doi:10.1017/S0022112092002040.

——, and C. L. Wolfe, 2009: Eddy-driven buoyancy gradients on eastern boundaries and their role in the thermocline. *J. Phys. Oceanogr.,* **39,** 1595–1614, doi:10.1175/2009JPO4063.1.

——, ——, and B. C. Ludka, 2010: Eastern-boundary contribution to the residual and meridional overturning circulations. *J. Phys. Oceanogr.,* **40,** 2075–2090, doi:10.1175/2010JPO4426.1.

Danabasoglu, G., and J. C. McWilliams, 1995: Sensitivity of the global ocean circulation to parameterizations of mesoscale tracer transports. *J. Climate,* **8,** 2967–2987, doi:10.1175/1520-0442(1995)008<2967:SOTGOC>2.0.CO;2.

Fasullo, J. T., and K. E. Trenberth, 2008: The annual cycle of the energy budget. Part II: Meridional structures and poleward transports. *J. Climate,* **21,** 2313–2325, doi:10.1175/2007JCLI1936.1.

Ferrari, R., and C. Wunsch, 2009: Ocean circulation kinetic energy: Reservoirs, sources, and sinks. *Annu. Rev. Fluid Mech.,* **41,** 253–282, doi:10.1146/annurev.fluid.40.111406.102139.

——, S. M. Griffies, A. J. G. Nurser, and G. K. Vallis, 2010: A boundary-value problem for the parameterized mesoscale eddy transport. *Ocean Modell.,* **32,** 143–156, doi:10.1016/j.ocemod.2010.01.004.

Garabato, A. C. N., K. L. Polzin, B. A. King, K. J. Heywood, and M. Visbeck, 2004: Widespread intense turbulent mixing in

the Southern Ocean. *Science,* **303,** 210–213, doi:10.1126/science.1090929.

Gent, P. R., and J. C. McWilliams, 1990: Isopycnal mixing in ocean circulation models. *J. Phys. Oceanogr.,* **20,** 150–155, doi:10.1175/1520-0485(1990)020<0150:IMIOCM>2.0.CO;2.

Gnanadesikan, A., 1999: A simple predictive model for the structure of the oceanic pycnocline. *Science,* **283,** 2077–2079, doi:10.1126/science.283.5410.2077.

Gordon, A. L., 1986: Interocean exchange of thermocline water. *J. Geophys. Res.,* **91** (C4), 5037–5046, doi:10.1029/JC091iC04p05037.

Griesel, A., and M. A. M. Maqueda, 2006: The relation of meridional pressure gradients to North Atlantic Deep Water volume transport in an ocean general circulation model. *Climate Dyn.,* **26,** 781–799, doi:10.1007/s00382-006-0122-z.

Haney, R. L., 1971: Surface thermal boundary condition for ocean circulation models. *J. Phys. Oceanogr.,* **1,** 241–248, doi:10.1175/1520-0485(1971)001<0241:STBCFO>2.0.CO;2.

Knorr, G., and G. Lohmann, 2003: Southern Ocean origin for the resumption of Atlantic thermohaline circulation during deglaciation. *Nature,* **424,** 532–536, doi:10.1038/nature01855.

Kuhlbrodt, T., A. Griesel, M. Montoya, A. Levermann, M. Hofmann, and S. Rahmstorf, 2007: On the driving processes of the Atlantic meridional overturning circulation. *Rev. Geophys.,* **45,** RG2001, doi:10.1029/2004RG000166.

Kunze, E., E. Firing, J. M. Hummon, T. K. Chereskin, and A. M. Thurnherr, 2006: Global abyssal mixing inferred from lowered ADCP shear and CTD strain profiles. *J. Phys. Oceanogr.,* **36,** 1553–1576, doi:10.1175/JPO2926.1.

Marotzke, J., 2000: Abrupt climate change and thermohaline circulation: Mechanisms and predictability. *Proc. Natl. Acad. Sci. USA,* **97,** 1347–1350, doi:10.1073/pnas.97.4.1347.

Marshall, J., and K. Speer, 2012: Closure of the meridional overturning circulation through Southern Ocean upwelling. *Nat. Geosci.,* **5,** 171–180, doi:10.1038/ngeo1391.

——, A. Adcroft, C. Hill, L. Perelman, and C. Heisey, 1997a: A finite-volume, incompressible Navier Stokes model for studies of the ocean on parallel computers. *J. Geophys. Res.,* **102** (C3), 5753–5766, doi:10.1029/96JC02775.

——, C. Hill, L. Perelman, and A. Adcroft, 1997b: Hydrostatic, quasi-hydrostatic, and nonhydrostatic ocean modeling. *J. Geophys. Res.,* **102** (C3), 5733–5752, doi:10.1029/96JC02776.

Munk, W., 1966: Abyssal recipes. *Deep-Sea Res. Oceanogr. Abstr.,* **13,** 707–730, doi:10.1016/0011-7471(66)90602-4.

——, and C. Wunsch, 1998: Abyssal recipes II: Energetics of tidal and wind mixing. *Deep-Sea Res. I,* **45,** 1977–2010, doi:10.1016/S0967-0637(98)00070-3.

Nikurashin, M., and G. Vallis, 2012: A theory of the interhemispheric meridional overturning circulation and associated stratification. *J. Phys. Oceanogr.,* **42,** 1652–1667, doi:10.1175/JPO-D-11-0189.1.

Prather, M. J., 1986: Numerical advection by conservation of second-order moments. *J. Geophys. Res.,* **91** (D6), 6671–6681, doi:10.1029/JD091iD06p06671.

Radko, T., and I. Kamenkovich, 2011: Semi-adiabatic model of the deep stratification and meridional overturning. *J. Phys. Oceanogr.,* **41,** 757–780, doi:10.1175/2010JPO4538.1.

——, I. V. Kamenkovich, and P.-Y. Dare, 2008: Inferring the pattern of the oceanic meridional transport from the air–sea density flux. *J. Phys. Oceanogr.,* **38,** 2722–2738, doi:10.1175/2008JPO3748.1.

Rahmstorf, S., 1996: On the freshwater forcing and transport of the Atlantic thermohaline circulation. *Climate Dyn.,* **12,** 799–811, doi:10.1007/s003820050144.

Redi, M. H., 1982: Oceanic isopycnal mixing by coordinate rotation. *J. Phys. Oceanogr.,* **12,** 1154–1158, doi:10.1175/1520-0485(1982)012<1154:OIMBCR>2.0.CO;2.

Rintoul, S. R., 1991: South Atlantic interbasin exchange. *J. Geophys. Res.,* **96** (C2), 2675–2692, doi:10.1029/90JC02422.

Robinson, A., and H. Stommel, 1959: The oceanic thermocline and the associated thermohaline circulation. *Tellus,* **11,** 295–308, doi: 10.1111/j.2153-3490.1959.tb00035.x.

Roemmich, D., and C. Wunsch, 1985: Two transatlantic sections: Meridional circulation and heat flux in the subtropical North Atlantic Ocean. *Deep-Sea Res.,* **32A,** 619–664, doi:10.1016/0198-0149(85)90070-6.

Rooth, C., 1982: Hydrology and ocean circulation. *Prog. Oceanogr.,* **11,** 131–149, doi:10.1016/0079-6611(82)90006-4.

Stommel, H., 1961: Thermohaline convection with two stable regimes of flow. *Tellus,* **13,** 224–230, doi:10.1111/j.2153-3490.1961.tb00079.x.

——, and A. B. Arons, 1959a: On the abyssal circulation of the world ocean—I. Stationary planetary flow patterns on a sphere. *Deep-Sea Res.,* **6,** 140–154, doi:10.1016/0146-6313(59)90065-6.

——, and ——, 1959b: On the abyssal circulation of the world ocean—II. An idealized model of the circulation pattern and amplitude in oceanic basins. *Deep-Sea Res.,* **6,** 217–218, doi:10.1016/0146-6313(59)90075-9.

Toggweiler, J. R., and B. Samuels, 1995: Effect of Drake Passage on the global thermohaline circulation. *Deep-Sea Res. I,* **42,** 477–500, doi:10.1016/0967-0637(95)00012-U.

——, and ——, 1998: On the ocean's large-scale circulation near the limit of no vertical mixing. *J. Phys. Oceanogr.,* **28,** 1832–1852, doi:10.1175/1520-0485(1998)028<1832:OTOSLS>2.0.CO;2.

Trenberth, K. E., and J. T. Fasullo, 2008: An observational estimate of inferred ocean energy divergence. *J. Phys. Oceanogr.,* **38,** 984–999, doi:10.1175/2007JPO3833.1.

Vallis, G. K., 2000: Large-scale circulation and production of stratification: Effects of wind, geometry, and diffusion. *J. Phys. Oceanogr.,* **30,** 933–954, doi:10.1175/1520-0485(2000)030<0933:LSCAPO>2.0.CO;2.

Weaver, A. J., O. A. Saenko, P. U. Clark, and J. X. Mitrovica, 2003: Meltwater pulse 1A from Antarctica as a trigger of the Bølling–Allerød warm interval. *Science,* **299,** 1709–1713, doi:10.1126/science.1081002.

Wolfe, C. L., and P. Cessi, 2009: Overturning in an eddy-resolving model: The effect of the pole-to-pole temperature gradient. *J. Phys. Oceanogr.,* **39,** 125–142, doi:10.1175/2008JPO3991.1.

——, and ——, 2010: What sets the strength of the mid-depth stratification and overturning circulation in eddying ocean models? *J. Phys. Oceanogr.,* **40,** 1520–1538, doi:10.1175/2010JPO4393.1.

——, and ——, 2011: The adiabatic pole-to-pole overturning circulation. *J. Phys. Oceanogr.,* **41,** 1795–1810, doi:10.1175/2011JPO4570.1.

——, ——, J. L. McClean, and M. E. Maltrud, 2008: Vertical heat transport in eddying ocean models. *Geophys. Res. Lett.,* **35,** L23605, doi:10.1029/2008GL036138.

Wunsch, C., 1998: The work done by the wind on the oceanic general circulation. *J. Phys. Oceanogr.,* **28,** 2332–2340, doi:10.1175/1520-0485(1998)028<2332:TWDBTW>2.0.CO;2.

Young, W. R., 2012: An exact thickness-weighted average formulation of the Boussinesq equations. *J. Phys. Oceanogr.,* **42,** 692–707, doi:10.1175/JPO-D-11-0102.1.